TECHNICAL ARTICLE

Microstructure and Sliding Wear Behavior of High Chromium Cast Iron Strengthened Low Carbon Steel Composite

Guofeng Yuan, Xiaogang Wang, Xiaoyu Zhu, and Peisheng Han

To improve the wear resistance of the low carbon steel (LCS), high chromium cast iron (HCCI) was embedded into LCS by the hot rolling technique. The macrostructure, microstructure characteristics, and sliding wear behavior of HCCI strengthened LCS composite were analyzed. After hot rolling, the brittle HCCI layers were broken and randomly dispersed in the LCS matrix. The area fraction of HCCI varied at different distances from the surface layer of the composite. Coarse M_7C_3 carbides in HCCI fractured, and there were unclosed pores and micro-cracks in the fractured carbides. The broken HCCI combined well with the LCS matrix without unbonded region or voids by mechanical and metallurgical bonding. Wear specimens with a larger area fraction of HCCI had better wear performance. During the sliding wear process, the HCCI randomly dispersed in the LCS matrix produced a shadow effect.

1. Introduction

Low carbon steel (LCS) is a widely applied material in modern industry. However, the low alloy steel or LCS has low hardness and poor wear resistance, which often leads to a shorter service life (Ref 1). Many studies in this field have been devoted to improving the hardness and wear resistance of the LCS surface through nitriding, carburizing, and plasma-electrolytic boriding treatment (Ref 2. Besides, some researchers have made attempts to increase the wear properties of the carbon steel by the surface coating technology, such as plasma cladding (Ref 1, 3), high-velocity oxy-fuel thermal spraying (HVOF) (Ref 4, 5), and laser cladding (Ref 6, 7). Another way to improve the wear resistance of a material is to add a hard reinforcing phase to the matrix (Ref 8-10).

Owing to the high-volume fraction of $(Fe,Cr)_7C_3$ carbides (Ref 11-13), high chromium cast iron (HCCI) has high hardness and good wear resistance, which contribute to its extensive application in wear-affected equipment and operating conditions (Ref 14-16). However, the hard and brittle chromium carbides have weakened the impact resistance of HCCI and restricted its further development (Ref 17, 18). A single metal material can no longer meet the requirements of practical application in some situations, and composite materials with distinctive properties have attracted the attention of considerable researchers. Recently, HCCI/LCS bimetals have been reported mainly as laminated metal composite materials. Gao et al. (Ref 19, 20) constructed a sandwich structure with solid-state LCS and HCCI through the hot compression bonding process. They observed the intergrowth between the LCS and HCCI when the bonding temperature was above 1100 °C. In addition, reducing the strain rate was beneficial to improve the bonding strength, and the thermomechanical treatment could refine the microstructure of HCCI and improve its wear properties. Similarly, the effect of bonding temperature on the bonding strength of HCCI and LCS was analyzed by Eroglu et al. (Ref 21), who concluded that the bonding strength was enhanced with the increasing bonding temperature and holding time. Xiong et al. (Ref 22, 23) investigated the influence of electromagnetic induction heating on the interface characteristics of HCCI/carbon steel composite plates prepared by liquid-solid casting. Due to the poor thermal deformation ability of HCCI, there are few studies on the preparation of HCCI/LCS composite materials by hot rolling or deforming the monolithic HCCI through hot rolling.

At present, a great number of studies have been done on the accumulative roll bonding of dissimilar metals, such as Mg/Al (Ref 24), Al/Cu (Ref 25), Ti/Al (Ref 26), Al/Steel (Ref 27), carbon steel and stainless steel (Ref 28, 29. In the accumulative roll bonding process, the hard layer will first neck down and fracture and be inserted into the soft component layer (Ref 30). Therefore, the HCCI is assumed to possibly disperse in the LCS composite through hot rolling HCCI and LCS in multiple layers. In this way, an HCCI reinforced LCS composite could be prepared. In this case, the hard HCCI may be considered as a reinforcing phase, which acts as a support during wear and prevents the cutting of debris and the spread of scratches, thus protecting the matrix from wear.

Guofeng Yuan, Engineering Research Center Heavy Machinery Ministry of Education, Taiyuan University of Science and Technology, Taiyuan 030024, China; and School of Mechanical Engineering, Anyang Institute of Technology, Anyang 455000, China; and **Xiaogang Wang, Xiaoyu Zhu,** and **Peisheng Han**, Engineering Research Center Heavy Machinery Ministry of Education, Taiyuan University of Science and Technology, Taiyuan 030024, China. Contact e-mail: wxg@tyust.edu.cn.

In the light of previous research, a seven-layer HCCI/LCS composite slab was hot-rolled to afford the HCCI-reinforced LCS matrix composite. The macrostructure of the composite was analyzed through three cross-sections. The microstructure was observed under the optical microscope (OM), scanning electron microscope (SEM), and transmission electron microscope (TEM). The sliding wear behavior of the composite was discussed.

2. Experimental

As-cast HCCI plates with high hardness and stiffness and commercial LCS plates with good toughness and ductility were used as the raw materials. The Vickers hardness and chemical composition of the raw materials are listed in Table 1.

The surfaces of LCS plates (width; 100 mm, length; 150mm, thickness; 2 mm) and HCCI plates (width; 100 mm, length; 150mm, thickness; 2.5 mm) were cleaned by descaling machined at first. The LCS and HCCI plates were alternately stacked, as shown in Fig. 1. That is to say, each HCCI plate was embedded between two LCS plates. After assembly, the volume fraction of HCCI in the laminate was 48.4%. It was established by Masahashi et al. (Ref 31 that the cladding by soft materials could effectively relieve stress and thus deform hard materials. The alternately stacked sheets edges were welded with a carbon steel package box. The air inside the slab was pumped out to achieve a vacuum degree of 1×10^{-3} Pa.

The composite slab was heated in the furnace at 1100 °C for 30 min and rolled immediately. Nine-pass rolling was carried out with the reduction rate per pass not exceeding 20%. The temperature of the slab would decrease after the multi-pass rolling. The surface temperature of the composite slab was detected by an infrared thermometer. The initial rolling temperature was ∼1080 °C and the temperature of the slab was reduced to ∼890 ºC after the sixth rolling processing. To prevent the low temperature of the slab from causing serious cracking of HCCI and affecting the formability of the composite plate, the slab was reheated up to 1100 °C and held for 10 min after the first six passes. Table 2 shows the variation of thickness and the pass reduction of the hot-rolled composite plate. The rolling speed was 0.2 m s^{-1} and the total reduction ratio was 75%.

The pin-on-disc configuration was adopted to investigate the sliding wear performance of the commercial LCS, as-cast HCCI, and the composite material. To get accurate results, each material was tested three times. The wear test samples were cut from the middle of the sheet along the rolling direction. The sliding wear test was carried out on the RD-TD section of the sample (see Fig. 2a). A 1 mm-, 1.5 mm-, and 2 mm-thick layers were removed from the surface of the test sample of the composite by the grinding machine, which was labeled as WT-1, WT-1.5, and WT-2, respectively. The sliding wear tests were carried out following the guidelines of the ASTM G99-05 standard (Ref 32). Before the test. the surface of the wear sample was polished to a roughness level of 0.8 μm (R_a) and cleaned up with ethanol. The test specimens were subjected to sliding wear for 30 min at a load of 50N, and the radius of the

Table 2 Pass reduction of the hot-rolled composite plate

Pass	Thickness, mm	Reduction, %
0	15.5	0
1	12.5	19.4
2	10.5	16
3	8.8	16.2
4	7.3	17
5	6	17.8
6	5	16.7
Reheated up to 1100 °C and held for 10min		
7	4.5	10
8	4	11.1
9	3.8	5

Table 1 Chemical compositions (wt%) and Vickers hardness (HV) of HCCI and LCS

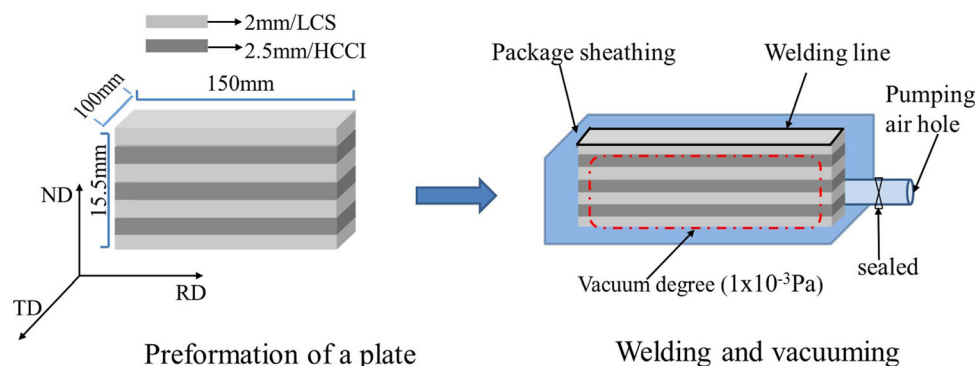| Material	C	Si	Cr	Mn	P	S	Mo	Ni	Fe	Hardness
HCCI	2.8	1.1	28	1.0	0.02	0.02	0.5	0.4	balance	755 ± 50
LCS	0.15	0.2	0.1	0.5	0.01	0.002	…	…	balance	170 ± 10

Fig. 1 Schematic diagram of the multilayer hot rolling (RD: rolling direction, ND: normal direction, TD: transverse direction)
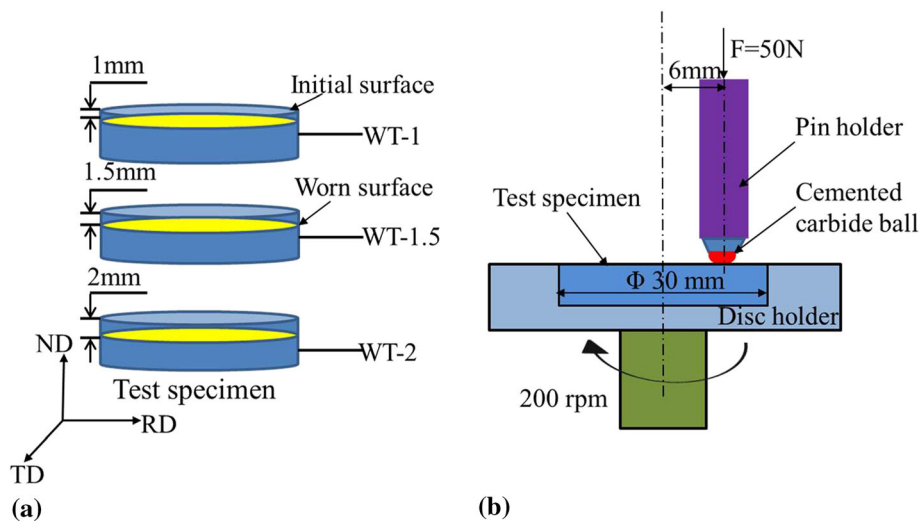
Fig. 2 (a) Wear specimens and their codes; (b) schematic diagram of the pin-on-disc apparatus
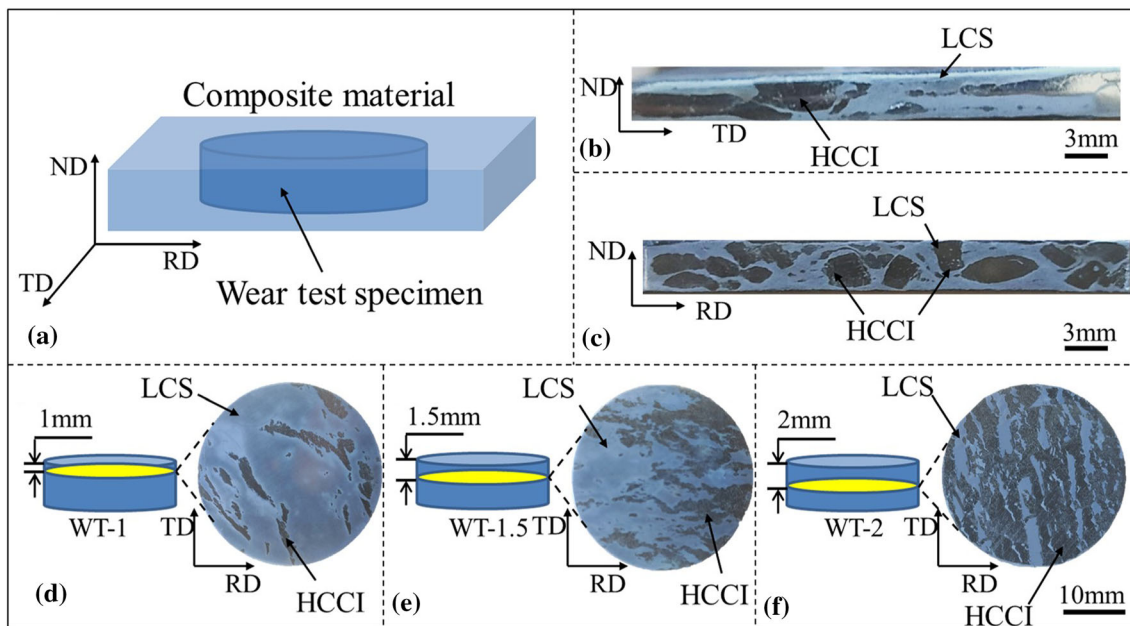

Fig. 3 Macroscopic photographs of different cross-sections of the composite: (a) samples, (b) TD-ND surface, (c) RD-ND surface, (d) RD-ND surface of WT-1, (e) RD-ND surface of WT-1.5, (f) RD-ND surface of WT-1.5

wear track was 6 mm, as shown in Fig. 2(b). The wear weight loss was measured by a precision electronic balance with an accuracy of ±0.0001g.

The microstructure of the composite was analyzed on the rolling direction-normal direction (RD-ND). The metallographic sample was ground, polished, and etched with a 4% nitric acid solution. The microstructure was observed by the optical microscope (OM), SEM (equipped with energy-dispersive spectroscopy (EDS)). The phase constitution of different wear test specimens was identified by high-resolution x-ray diffractometer (XRD) at a voltage of 40 kV. The deformed carbide of HCCI was observed by the transmission electron microscope (TEM).

3. Results and Discussion

3.1 Random Distribution of HCCI

Figure 3 displays the macrostructure of the composite material. In the composite, the layered structure of LCS and HCCI was no longer visible. The laminated HCCI layers were broken during the hot-rolling deformation and wrapped by the soft LCS. On the RD-ND surface, the broken HCCI was an uneven block structure, which was randomly distributed in the LCS. However, the HCCI was an intermittent long strip on the RD-TD surface. In the rolling process, the cracks of HCCI were mainly perpendicular to the rolling direction, therefore, the HCCI was distributed more uniformly on the RD-ND surface

than on the RD-TD surface. As indicated in Fig. 3(d)-(f), the HCCI was irregularly dispersed in the LCS matrix and its macrostructure was shaped as clouds on the RD-TD surface. The macroscopic photographs of the RD-TD surface were processed by the software "ImagePro" and the area fractions of HCCI on different surfaces are shown in Fig. 4. The area fraction of HCCI was different on three cross-sections. In general, the size of the crushed HCCI in the LCS matrix was uneven and its distribution was random.
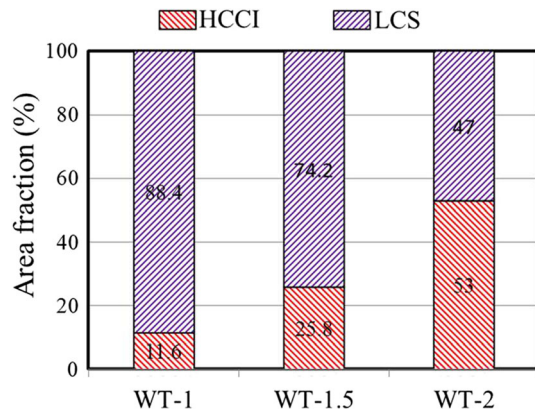
3.2 Microstructure and Forming Mechanism of the Composite Material

Figure 5 shows the microstructure of the composite. The interface of the two metals is undulating and corrugated. The layers of HCCI and LCS were no longer continuous. The brittle HCCI layers fractured and broke into granules, and necking fractures could be observed. A part of the HCCI particles was completely coated with LCS, as suggested in Fig. 5(b). No defect such as cracks or unbonded areas was observed. The adjacent LCS layers were bonded together in certain areas and
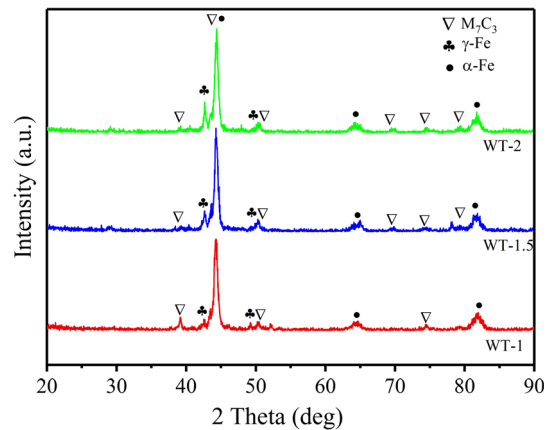

Fig. 4 Area fraction of HCCI and the LCS matrix of different surfaces

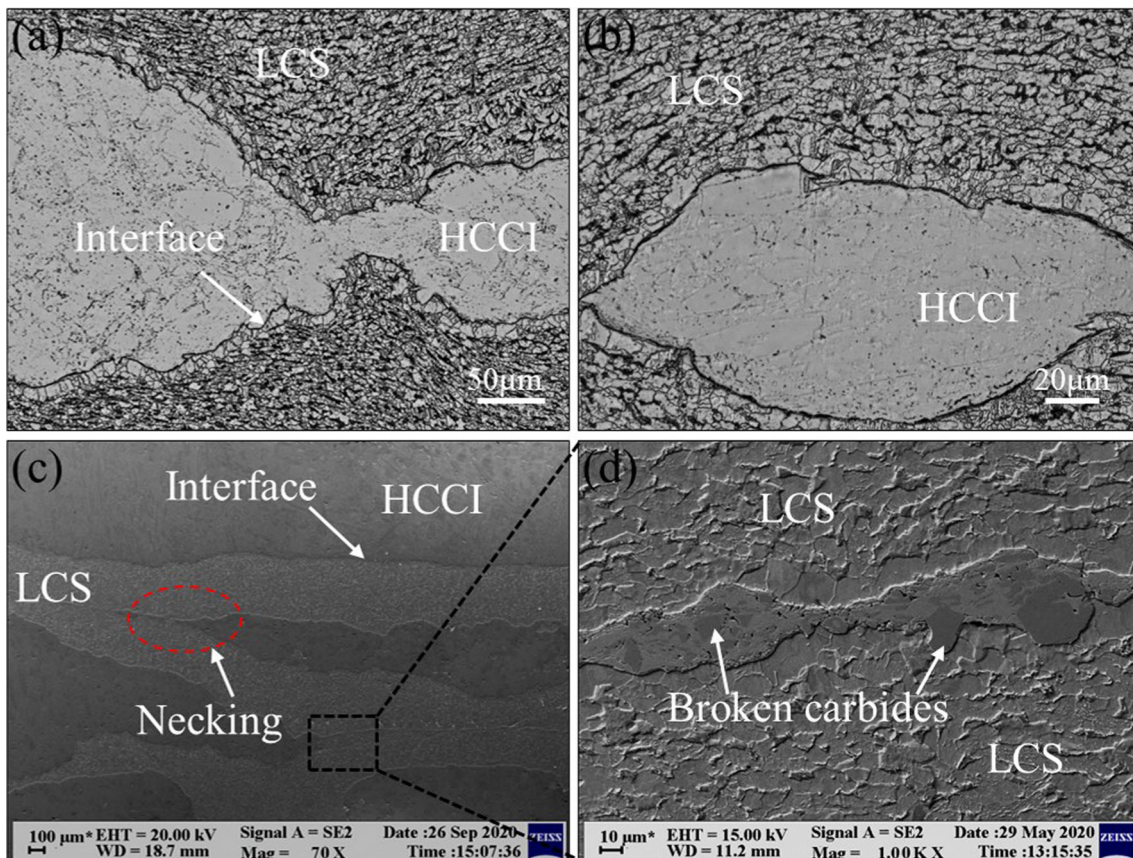**Fig. 6** XRD patterns of the composite of different wear test specimen

Fig. 5 Microstructure of the composite material in the RD-ND direction: (a) and (b) OM images, (c) and (d) SEM images
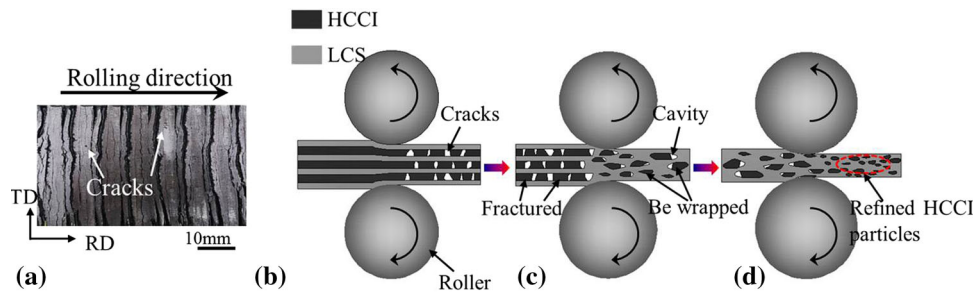
Fig. 7 (a) Macroscopic photograph of HCCI after hot rolling, (b-c) schematic diagram of the rolling forming of the composite material
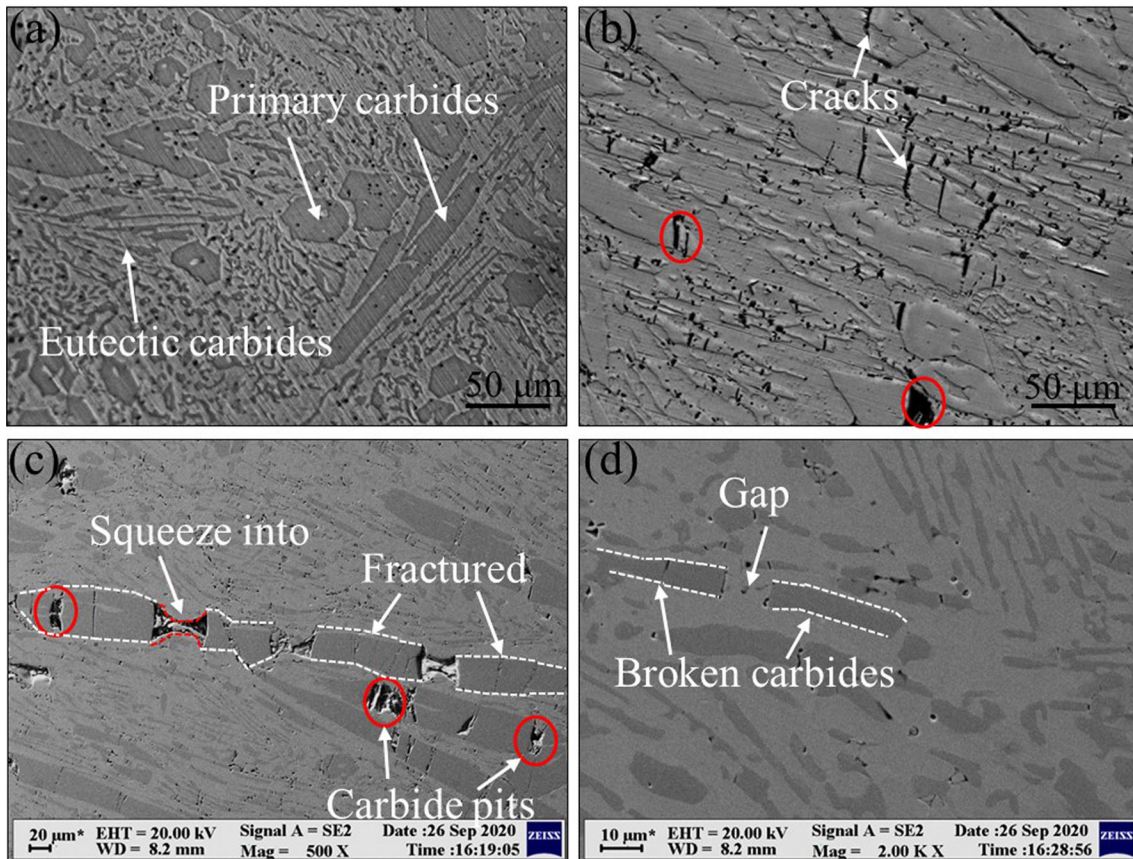

Fig. 8 OM and SEM micrographs of HCCI on the RD-ND section: (a) OM micrographs before hot rolling, (b) OM micrographs after hot rolling, (c) and (d) SEM micrographs after hot rolling

there were broken HCCI particles between the two layers (see Fig. 5d). The broken carbides in HCCI were observed in the HCCI particles. The morphology and distribution of the broken HCCI particles were irregular and the size of the HCCI particles varied greatly.

XRD was used to determine the phase constitutions of the surface of different wear test specimens. It can be seen that the three wear test specimens contain α-Fe, γ-Fe, and M_7C_3 carbide as shown in Fig. 6. The LCS consists of ferrite and pearlite, while the microstructure of HCCI is characterized by large hexagonal primary M_7C_3 (where M includes Fe and Cr) carbide in a matrix of martensite with retained austenite (Ref 19).

Because the crystal structure of ferrite is similar to that of martensite, the peak values shown by α-Fe in XRD measurements contain both martensite and ferrite.

The thermal deformation capacity of the monolithic HCCI plate is poor (Ref 33), and there were many cracks on the surface of HCCI after hot the rolling deformation (see Fig. 7a). During the hot rolling process, the easily deformed LCS could fill the cracks of HCCI, thereby improving the continuity of the sheet. The forming mechanism of the composite is described in Fig. 7(b)-(c). In the early stage of rolling, the HCCI layers between LCS layers broke and formed a lot of cracks, and the LCS layers deformed simultaneously to promote the propaga-
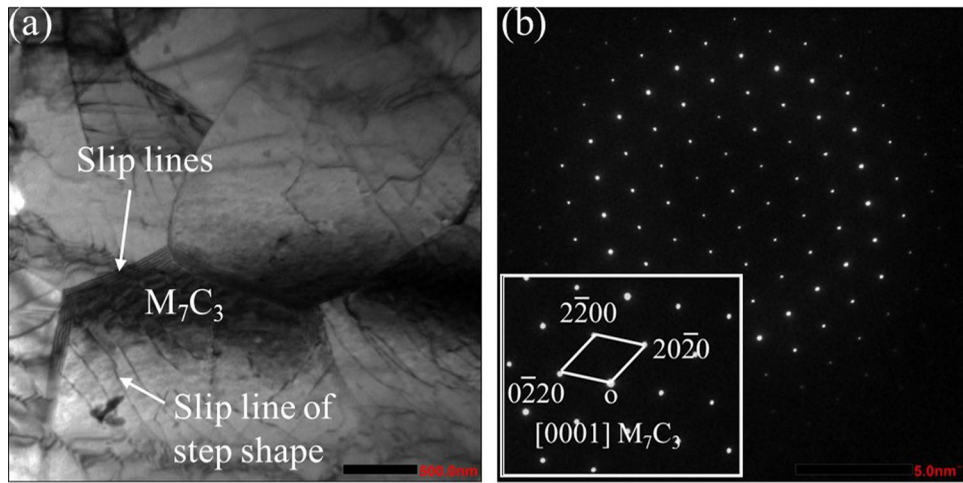
Fig. 9 Typical bright-field TEM image of M_7C_3 carbides in HCCI after hot rolling and the corresponding SADP

tion of the cracks (see Fig. 7b). With the increase of rolling passes, the soft LCS squeezed into the cracks under the action of the rolling force. Some of the cracks were fully coated with LCS, but some were not filled by LCS and formed cavities (see Fig. 7c). Furthermore, the blocky HCCI would be further broken and refined by the rolling force and distributed in the LCS matrix (see Fig. 7d). As a result, the two materials were embedded with each other until all the cavities were filled with fresh metal.

3.3 Microstructure of the HCCI After Hot Rolling

Figure 8 discusses the effect of hot rolling on the microstructure of HCCI. Figure 8(a) presents the as-cast microstructure of HCCI before hot rolling. The primary M_7C_3 carbides were hexagonal or irregular blocks of different sizes. The fine rods of eutectic carbides were distributed around the primary carbides.

After hot rolling, some micro-cracks were observed in the primary carbides, as can be seen from Fig. 8(b), (c). The rod-shaped Cr-carbides were fractured, between which some pits were formed. The gap between the fractured carbides was filled by the matrix (see Fig. 8c, d), but those not completely filled by the matrix would form cavities. Pei et al. (Ref 34) reported an excellent self-healing effect of the austenite softened at high temperature on the carbide gaps and fractures. The primary M_7C_3 carbides tend to deform along the rolling direction. It was claimed by Gao et al. (Ref 19, 20) that the orientation of carbides in HCCI rotated about 90° under hot compression, and the carbides were obviously refined after hot rolling. As was demonstrated by Filipovic et al. (Ref 35) and Tang et al. (Ref 11), the refinement of carbides was conducive to better wear resistance while protecting the matrix.

Figure 9 is the typical bright-field TEM image of M_7C_3 carbides in HCCI after hot rolling. The hexagonal carbides were identified as M_7C_3 by the corresponding SADP (see Fig. 9b). During hot rolling, the brittle M_7C_3 carbides underwent minor plastic deformation and deformed with the flow of the matrix. Parallel slip lines could be observed at the edges of the carbides. Moreover, there were step-like slip lines

in the M_7C_3 carbides, as shown in Fig. 9(a). It was attributed to the slip motion of the dislocation. The above results indicated that plastic deformation of the M_7C_3 carbide also took place, and the mechanism was the dislocation slip.

3.4 Microstructure Characteristics of the Bonding Interface

The interface structure and interface diffusion are important for the mechanical properties of the composite material (Ref 36). As shown in Fig. 10(a), there were neither unbonded areas nor micro-voids detected at the interface. The bond line of the two metals was wave-shaped and the wave joint could improve the bonding strength (Ref 37, 38). However, rod-shaped oxides (circled in red in Fig. 10a, b) were distributed on the binding interface of the two metals. The EDS point analysis (see Fig. 10c) was carried out on the black oxides around the yellow arrow area in Fig. 10(b). It indicated that the oxides contained a large amount of Si and O atoms. The EDS mapping analysis of bonding interface results (see Fig. 10h) shows that the black stripe substance contains more Si elements. The residual oxygen elements adsorbed at the clearance of the surface reacted with Si, Cr, and Fe elements of the plate surface during the heating stage, thereby forming some thin oxides detrimental to the bonding strength at the interface before rolling deformation (Ref 39). Besides, thin oxide film could also form on the surface of the slab during the mechanical grinding and welding process. With the progress of the rolling deformation, the oxides at the interface broke into particles or short rods.

A black band was formed at the bonding interface (see Fig. 10a), and it could be regarded as a diffusion zone. Figure 10(d) represents the diffusion zone in detail; it can be identified as lamellar pearlite with a width of 3-5 μm. A ferrite band of approximately 20 μm width was formed at the LCS region, which suggested the occurrence of decarburization on LCS (Ref 40).

Figure 10(e), (f) show the results of EDS line analysis of the bonding interface, at which Cr, Mn, and Fe elements diffused. The diffusion zone of Cr, Fe, and Mn was determined to be 8-11μm. Figure 10(g), (h) show the results of the EDS mapping analysis of the bonding interface. The Fe atoms are mainly
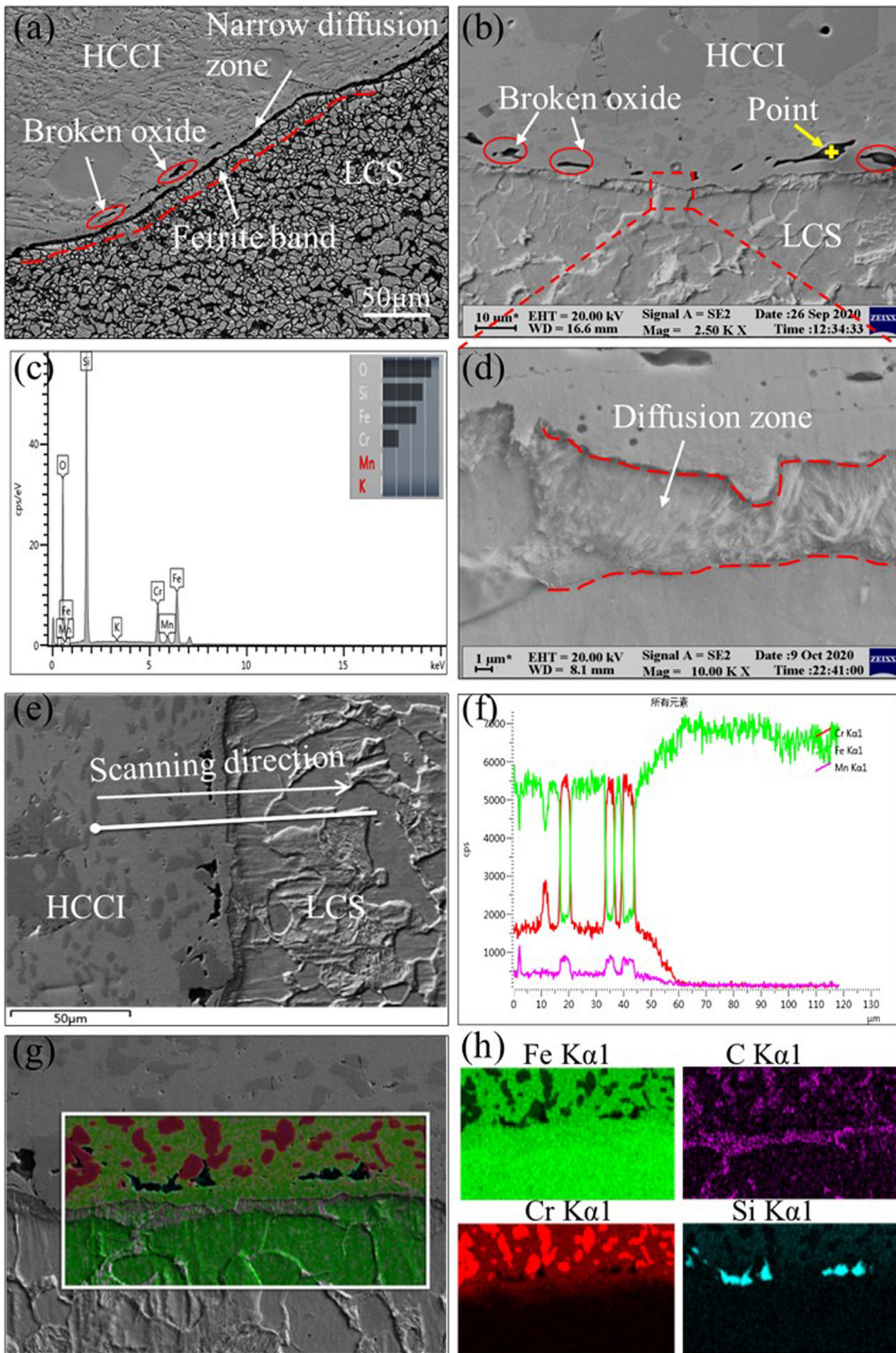
Fig. 10 Micrographs and EDS analysis of the interface: (a) OM micrograph, (b) SEM micrograph, (c) EDS point analysis take from the yellow arrow area in b, (d) SEM details of the diffusion zone, (e) and (f) EDS line analysis at the interface, (g) and (h) EDS mapping analysis

distributed in the side of LCS and the matrix of HCCI. Cr atoms are mainly distributed in the M$_7$C$_3$ carbides and the HCCI matrix. The Cr content gradually decreased in the transition zone. The diffusion of alloy elements revealed the formation of metallurgical bonds at the interface, and it would effectively connect the LCS and HCCI.

3.5 Wear Response

The average wear weight loss of the wear test specimen is illustrated in Fig. 11. It can be seen that the weight loss of the composite material was between that of LCS and HCCI. Concretely, the wear specimens with a larger area fraction of HCCI had better wear performance. The embedding of randomly distributed HCCI could effectively improve the wear resistance of LCS, and the wear specimen with a larger area fraction of HCCI had better wear performance. On the whole, the wear performance of the dispersed HCCI reinforced LCS composite was higher than that of LCS.

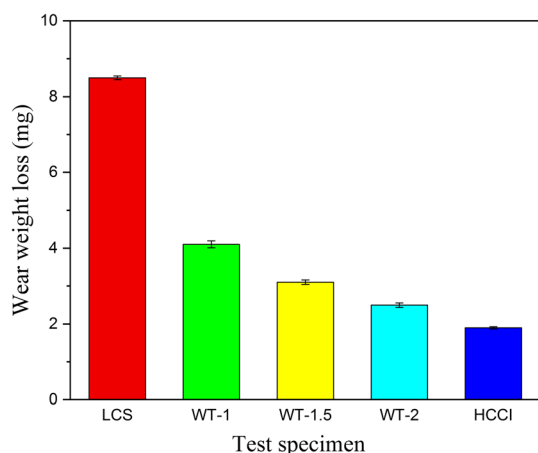As suggested by the macroscopic images of the wear track of the WT-1.5 test specimen in Fig. 12, the width and depth of the entire wear track were uneven. The scratch-made by the pin on the LCS side was notably wider than that on the HCCI side (see Fig. 12b). On account of the different hardness between the two materials, they showed different wear morphologies under the same wear condition.

The surface topographies of the three tested specimens are revealed in Fig. 13. During the sliding wear test, the two metal materials are in a smooth transition (see Fig. 13a, and d). No nubbly HCCI was found spalling from the LCS substrate throughout the wear track, which indicated a high bonding strength between the two materials. The wear morphologies of the HCCI side and LCS side differed markedly. The wear pattern of the LCS side was mainly plow wear, and many parallel furrows were formed, as shown in Figs. 13(c) and 14(a). On the HCCI side, debris and delamination can be observed on the worn surface, which is formed by the combined effect of plastic deformation, fatigue, and fracture (Ref 41). The fracture and shedding of hard carbides was the dominant wear mechanism of the HCCI side, and many carbide pits formed on the worn surface (see Fig. 13b, and e). Moreover, oxidative wear occurred on the HCCI during the sliding process. Figure 13(h1)-(h3) are EDS map results of O, Fe, and Cr atoms on the worn surface of WT-2 specimen. The oxide film is mainly distributed in the matrix of HCCI. The fracture and crushing of Cr-carbides on the worn surface can be clearly observed from the EDS result of Cr atoms, as shown in Fig. 13(h1).

The DM micrographs of the WT-1.5 test specimen are revealed in Fig. 14. It can be seen from Fig. 14(a) and (b) that the surface topographies of the two metals are obviously different. Figure 14(c) and (d) show the DM micrographs of the wear track at the bonding interface. It can be seen that the scratch deepened along the wear direction from HCCI sied to LCS side (see Fig. 14c). The depth of the scratch gradually deepened and changed gently. However, trenches were formed on LCS side near the HCCI as the wear pin moved from LCS side to HCCI side. Figure 14(e) shows the depth profiles of the wear tracks at the interface. When the wear direction was different, the trace distribution of the scratch depth at the interface was different.

The wear mechanism of the wear track at the bonding interface is elucidated in Fig. 15. During the sliding wear process, the hard HCCI, which can be considered as a reinforcer, was slightly convex while the soft LCS was slightly
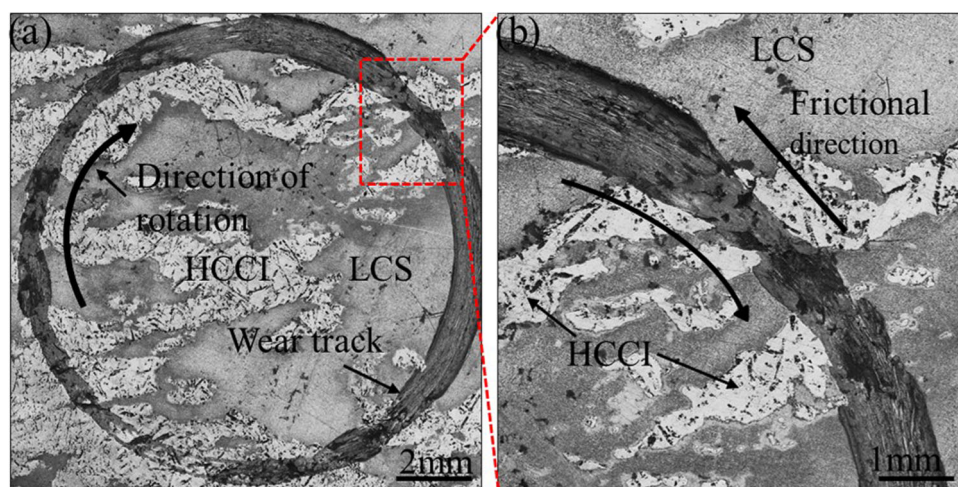

Fig. 11 Wear weight loss of the wear test specimen

Fig. 12 Macroscopic images of the wear track: (a) the overall wear track of WT-1.5 test specimen, (b) partial enlarged detail of the wear track
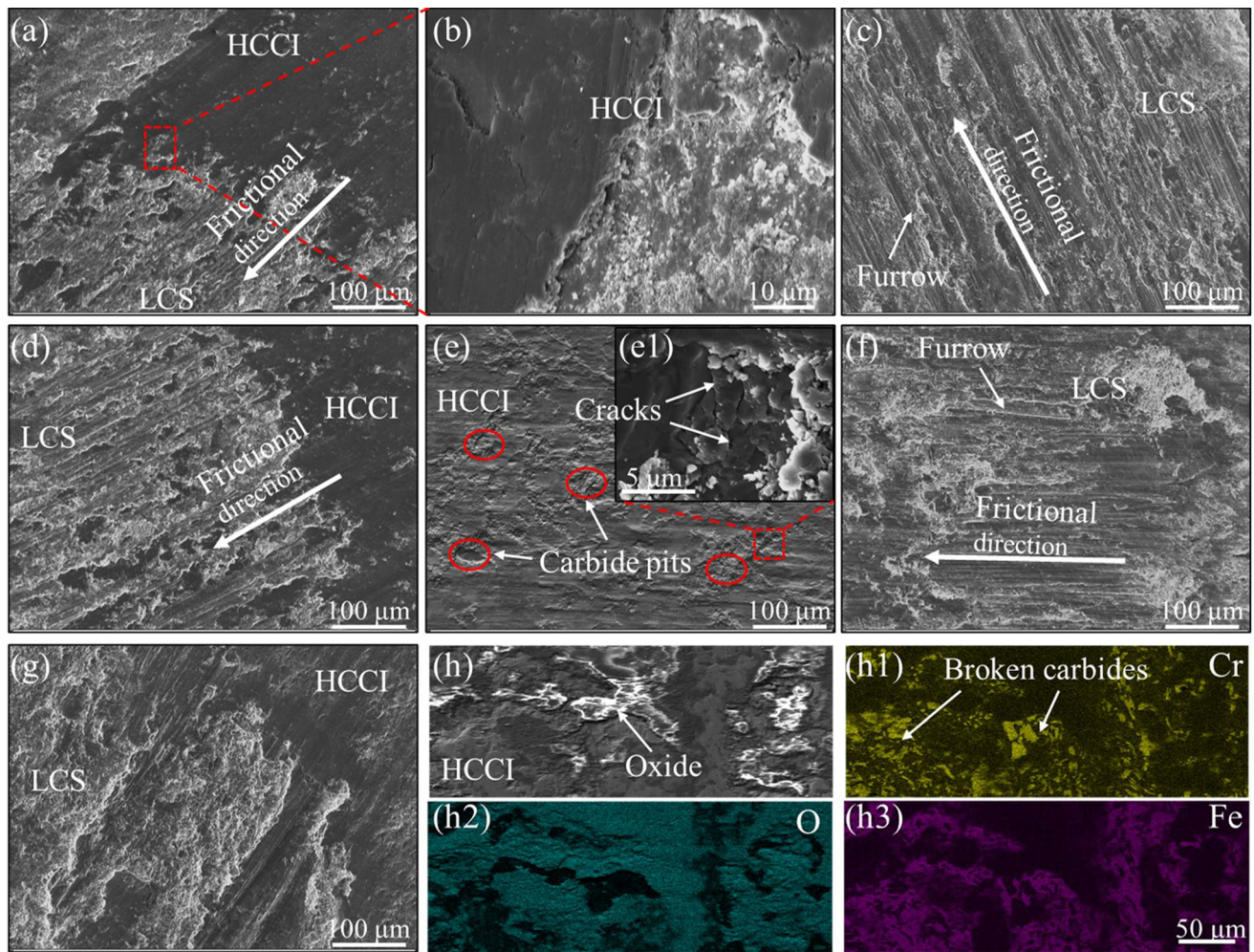
Fig. 13 SEM micrographs of the worn surface of the composite specimens: (a)-(c) WT-1 specimen, (d)-(f) WT-1.5 specimen, (g) and (h) WT-2 specimen, (h1)-(h3) are the EDS map analysis of h

sunken, as shown in Fig. 15(a). Due to the sustaining capacity of the randomly distributed HCCI on the worn surface of composite, the LCS behind the HCCI along the friction direction carried a reduced load. The bulgy HCCI was like a shadow, protecting the LCS (Ref 42). The wear profile of LCS near the HCCI side was an inclined surface, and the depth of the grinding mark increased gradually and tended to be stable. When the grinding pin moved from the softer matrix to the reinforcer, the convex HCCI suffered a greater impact, which accelerated the wear of the reinforcer and therefore weakened the shadow effect of HCCI, as shown in Fig. 15(b).

4. Conclusions

In this paper, an HCCI-strengthened LCS composite material was fabricated by hot rolling process, and its microstructure and sliding wear behavior were analyzed. The following conclusions were made from this work.

(1) The laminated HCCI was necked and broken during hot rolling, and finally wrapped by the LCS matrix. The crushed HCCI varying in size and shape was randomly distributed in the LCS. The area fraction of HCCI was different at different distances from the surface layer of the composite.

(2) The primary M_7C_3 carbides of HCCI were broken and refined, while micro-cracks and carbide pits could be observed. The LCS and HCCI were well connected, without unbonded regions. Element diffusion occurred at the interface and metallurgical bonds were formed. The diffusion zone was fine lamellar pearlite with a width of 3-5 μm.

(3) Wear specimens with a larger area fraction of HCCI had better wear performance. The worn surfaces of the two materials differed in depth and width. The hard HCCI was convex during the sliding wear process and produced a shadow effect, thereby protecting and supporting the soft LCS.
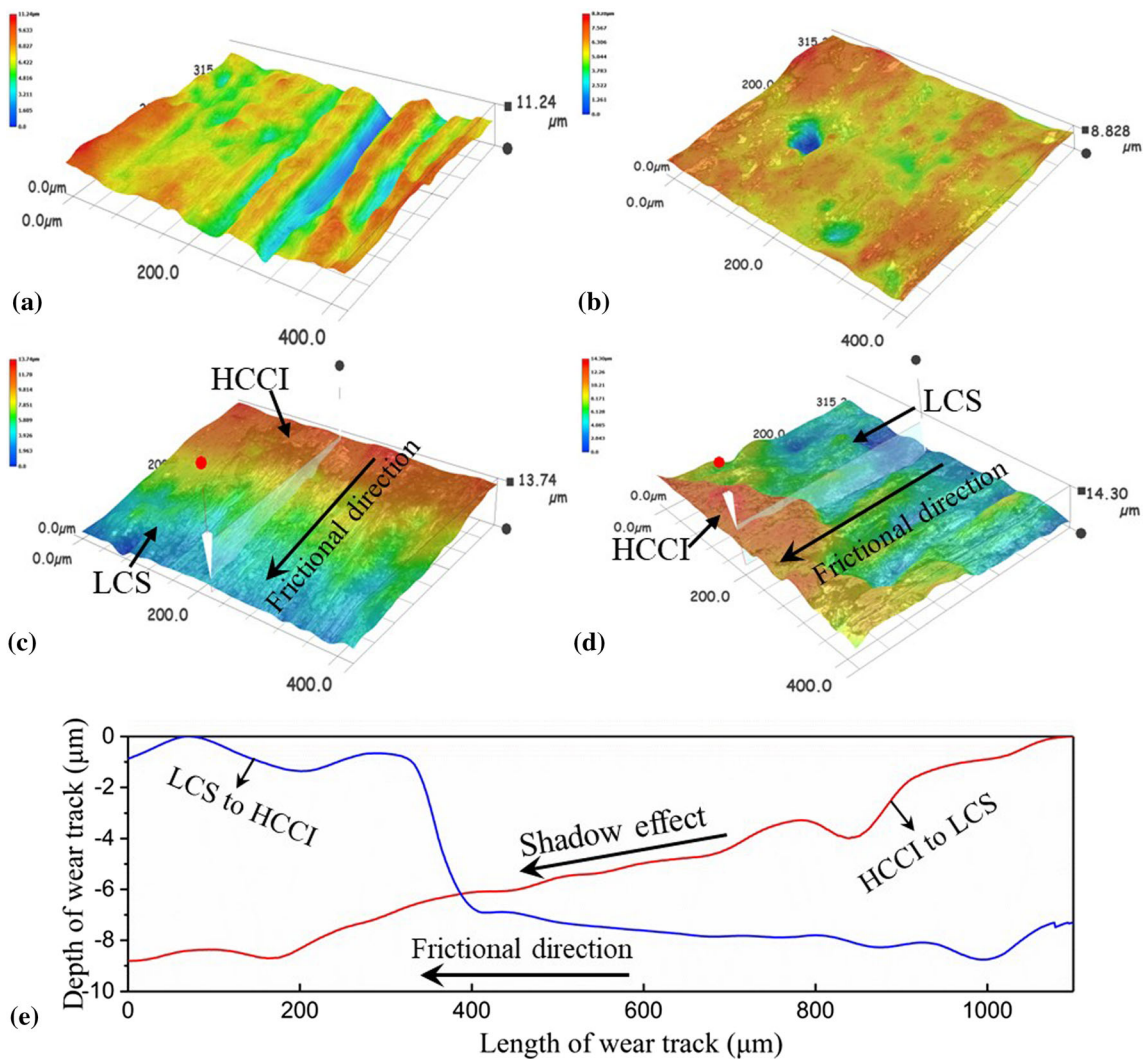
Fig. 14 DM micrographs of the wear track of WT-1.5 test specimen: (a) LCS side, (b) HCCI side, (c) and (d) the bonding interface, (e) depth profiles of the wear tracks at the interface
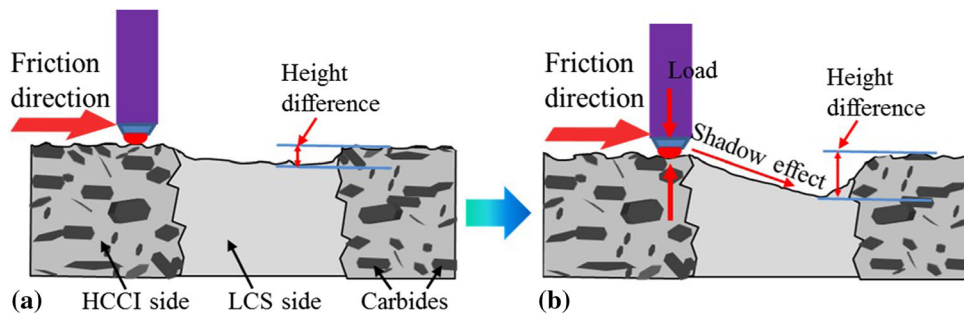

Fig. 15 Schematic diagram of the wear track

References

1. J.J. Yuan, Q.Z. Wang, X.Y. Liu, S.M. Lou, Q. Li, and Z.M. Wang, Microstructures and High-Temperature Wear Behavior of NiAl/WC-Fex Coatings on Carbon Steel by Plasma Cladding, *J. Alloys. Compd.*, 2020, **842**, 155850. https://doi.org/10.1016/j.jallcom.2020.155850

2. V.S. Belkin, P.N. Belkin, B.L. Krit, N.V. Morozova, and S.A. Silkin, Increasing Wear Resistance of Low-Carbon Steel by Anodic Plasma-Electrolytic Nitroboriding, *J. Mater. Eng. Perform.*, 2020, **29**, p 564–572. https://doi.org/10.1007/s11665-019-04521-1

3. M. Beyhaghi, M. Kashefi, A. Kiani-Rashid, J. Vahdati Khaki, and S. Jonsson, In-Situ Synthesis of Nanostructured NiAl-Al$_2$O$_3$ Composite Coatings on Cast Iron Substrates by Spark Plasma Sintering of Mechanically Activated Powders, *Surf. Coating. Technol.*, 2015, **272**, p 254–267.

4. G. Bolelli, B. Bonferroni, J. Laurila, L. Lusvarghi, A. Milanti, K. Niemi, and P. Vouristo, Micromechanical Properties and Sliding Wear Behaviour of HVOF-Sprayed Fe-Based Alloy Coatings, *Wear*, 2012, **276**, p 29–47. https://doi.org/10.1016/j.wear.2011.12.001

5. O. Culha, E. Celik, N.F. Ak Azem, I. Birlik, M. Toparli, and A. Turk, Microstructural, Thermal and Mechanical Properties of HVOF Sprayed Ni–Al-Based Bond Coatings on Stainless Steel Substrate, *J. Mater. Process. Technol.*, 2008, **204**, p 221–230. https://doi.org/10.1016/j.jmatprotec.2007.11.036

6. C. Zhu, B. Zhang, and S. Zheng, Laser Cladding Nickel-Titanium Carbide Composite Coating on a 45 Carbon Steel: Preparation, Microstructure and Wear Behavior, *Materialwiss Werkstofftech*, 2020, **51**, p 247–256. https://doi.org/10.1002/mawe.201900037

7. C.M. Lin, W.Y. Kai, C.Y. Su, and K.H. Key, Empirical Alloys-by-Design Theory Calculations to the Microstructure Evolution Mechanical Properties of Mo-Doped Laser Cladding NiAl Composite Coatings on Medium Carbon Steel Substrates, *J. Alloys. Compd.*, 2017, **702**, p 679–686. https://doi.org/10.1016/j.jallcom.2017.01.278

8. X.G. Sun, Y. Wang, D.Y. Li, and G.D. Wang, Modification of Carbidic Austempred Ductile Iron with Nano Ceria for Improved Mechanical Properties and Abrasive Wear Resistance, *Wear*, 2013, **301**, p 116–121. https://doi.org/10.1016/j.wear.2012.12.018

9. J.K. Kaleicheva, V. Mishev, Wear Resistance of Austempered Ductile Iron with Nanosized Additives, *IOP Conference Series: Materials Science and Engineering*, 2018, **295**, 012034. doi:https://doi.org/10.1088/1757-899X/295/1/012034

10. B.X. Wang, W.W. Cui, F. Qiu, W.H. Du, Y.B. Chen, and G.C. Barber, Pearlitic Structure and Wear Properties of Graphite Cast Iron Reinforced with Biphase TiC-TiB2 Nanoparticles, *Surf. Topogr. Metrol. Prop.*, 2020, **8**, p 045024.

11. X.H. Tang, R. Chung, D.Y. Li, B. Hinckley, and K. Dolman, Variations in Microstructure of High Chromium Cast Irons and Resultant Changes in Resistance to Wear, Corrosion and Corrosive Wear, *Wear*, 2009, **267**, p 116–121. https://doi.org/10.1016/j.wear.2008.11.025

12. Y. Wang, J.F. Gou, R.Q. Chu, D.X. Zhen, and S.Y. Liu, The Effect of Nano-Additives Containing Rare Earth Oxides on Sliding Wear Behavior of High Chromium Cast Iron Hardfacing Alloys, *Tribol. Int.*, 2004, **85**, p 32–40. https://doi.org/10.1016/j.matchemphys.2003.11.037

13. X.J. Wu, J.D. Xing, H.G. Fu, and X.H. Zhi, Effect of Titanium on the Morphology of Primary M$_7$C$_3$ Carbides in Hypereutectic High Chromium White Iron, *Mater. Sci. Eng. A*, 2007, **457**, p 180–185. https://doi.org/10.1016/j.msea.2006.12.006

14. F. Liu, Y.H. Jiang, H. Xiao, and J. Tan, Study on Fragmentation and Dissolution Behavior of Carbide in a Hot-Rolled Hypereutectic High Chromium Cast Iron, *J. Alloy. Compd.*, 2015, **618**, p 380–385. https://doi.org/10.1016/j.jallcom.2014.07.131

15. I. Fernández, and F.J. Belzunce, Wear and Oxidation Behaviour of High-Chromium White Cast Irons, *Mater. Charact.*, 2008, **59**, p 669–674. https://doi.org/10.1016/j.matchar.2007.05.021

16. A. Bedolla Jacuinde, and W.M. Rainforth, The Wear Behaviour of High-Chromium White Cast Irons as a Function of Silicon and MISCHMETAL CONTENT, *Wear*, 2001, **250**, p 449–461. https://doi.org/10.1016/S0043-1648(01)00633-0

17. K.H.Z. Gah, and D.V. Doane, Optimizing Fracture Toughness and Abrasion Resistance in White Cast Irons, *Metall. Trans. A.*, 1980, **11**, p 613–620. https://doi.org/10.1007/BF02670698

18. I.R. Sare, Abrasion Resistance and Fracture Toughness of White Cast Irons, *Mater. Sci. Tech-Lond.*, 2013, **19**, p 412–419. https://doi.org/10.1179/030716979803276228

19. X.J. Gao, Z.Y. Jiang, D.B. Wei, S.H. Jiao, and B. Kosasih, Effect of Thermomechanical Treatment on Sliding Wear of High-Cr Cast Iron with Large Plasticdeformation, *Tribol. Int.*, 2015, **92**, p 117–125. https://doi.org/10.1016/j.triboint.2015.06.002

20. X.J. Gao, Z.Y. Jiang, D.B. Wei, S.H. Jiao, D.F. Chen, J.Z. Xu, X.M. Zhang, and D.Y. Gong, Effects of Temperature and Strain Rate on Microstructure and Mechanical Properties of High Chromium Cast Iron/Low Carbon Steel Bimetal Prepared by Hot Diffusion-Compression Bonding, *Mater. Des.*, 2014, **63**, p 650–657. https://doi.org/10.1016/j.matdes.2014.06.067

21. M. Eroglu, and B. Kurt, Diffusion Bonding Between High Chromium White Iron and Low Carbon Steel, *Mater. Sci. Tech-Lond.*, 2007, **23**, p 171–176. https://doi.org/10.1179/174328407X154202

22. B.W. Xiong, C.C. Cai, H. Wan, and B.P. Lu, Fabrication of High Chromium Coast Iron and Medium Carbon Steel Bimetal by Liquid-Solid Casting in Electromagnetic Induction Field, *Mater. Des.*, 2011, **32**, p 2978–2982. https://doi.org/10.1016/j.matdes.2011.01.006

23. B.W. Xiong, C.C. Cai, H. Wan, and B.P. Lu, Effect of Volume Ratio of Liquid to Solid on the Interfacial Microstructure and Mechanical Properties of High Chromium Cast Iron and Medium Carbon Steel Bimetal, *J. Alloy. Compd.*, 2011, **509**, p 6700–6704.

24. K. Wu, H. Chang, E. Maawad, H.G. Brokmeier, and M.Y. Zheng, Microstructure and Mechanical Properties of the Mg/Al Laminated Composite Fabricated by Accumulative Roll Bonding, ARB), *Mater. Sci. Eng. A*, 2010, **527**, p 2073–2078. https://doi.org/10.1016/j.msea.2010.02.001

25. M.R. Toroghinejad, R. Jamaati, J. Dutkiewicz, and J.A. Szpunar, Investigation of Nanostructured Aluminum/Copper Composite Produced by Accumulative Roll Bonding and Folding Process, *Mater. Des.*, 2013, **51**, p 274–279. https://doi.org/10.1016/j.matdes.2013.04.002

26. M. Huang, C. Xu, G.H. Fan, E. Maawad, W.E. Gan, L. Geng et al., Role of Layered Structure in Ductility Improvement of Layered Ti-Al Metal Composite, *Acta. Mater.*, 2018, **153**, p 235–249. https://doi.org/10.1016/j.actamat.2018.05.005

27. M. Talebian, and M. Alizadeh, Manufacturing Al/steel Multilayered Composite by Accumulative Roll Bonding and the Effects of Subsequent Annealing on the Microstructural and Mechanical Characteristics, *Mater. Sci. Eng. A.*, 2014, **590**, p 186–193. https://doi.org/10.1016/j.msea.2013.10.026

28. R. Cao, X.K. Zhao, Y. Ding, X.B. Zhang, X.X. Jiang, Y.J. Yan, and J.H. Chen, Effects of the Rolling Temperature on Microstructure and Mechanical Properties of 2Cr13/316L Laminated Composites Prepared by Accumulative Roll-Bonding, ARB), *Mater. Charact.*, 2018, **139**, p 153–164. https://doi.org/10.1016/j.matchar.2018.03.001

29. J.T. Zou, S.L. Li, Y.N. Wei, and S.H. Liang, Research of the Bonded Interface of Cu9Al4Fe/1Cr18Ni9Ti Stainless Steel Bimetallic Composite, *Vacuum*, 2017, **146**, p 266–273. https://doi.org/10.1016/j.vacuum.2017.10.005

30. J.M. Lee, B.R. Lee, and B.S. Kang, Control of Layer Continuity in Metallic Multilayers Produced by Deformation Synthesis Method, *Mater. Sci. Eng. A*, 2005, **406**, p 95–101. https://doi.org/10.1016/j.msea.2005.06.030

31. N. Masahashi, S. Watanabe, S. Hanada, K. Komatsu, and G. Kimura, Fabrication of Iron Aluminum Alloy/Steel Laminate by Clad Rolling, *Metall. Mater. Trans. A.*, 2006, **37**, p 1665–1673. https://doi.org/10.1007/s11661-006-0108-9

32. Standard test method for wear testing with a pin-on-disk apparatus. ASTM Standard G99-05, 2010

33. J.Z. Xu, X.J. Gao, Z.Y. Jiang, and D.B. We, A Comparison of Hot Deformation Behavior of High-Cr white Cast Iron and High-Cr White Cast Iron/Low Carbon Steel Laminate, *Steel. Res. Int.*, 2016, **87**, p 780–788. https://doi.org/10.1002/srin.201500234

34. Y. Pei, R.B. Song, Y.C. Zhang, L. Huang, C.H. Cai, W. Wen, Z.Y. Zhao, P. Yu, S.Y. Quan, S.R. Su, and C. Chen, The Relationship Between Fracture Mechanism and Substructures of Primary M7C3 Under the Hot Compression Process of Self-Healing Hypereutectic High Chromium Cast Iron, *Mater. Sci. Eng. A*, 2020, **779**, 139150. https://doi.org/10.1016/j.msea.2020.139150

35. M. Filipovic, Z. Kamberovic, M. Korac, and M. Gavrilovski, Correlation of Microstructure with the Wear Resistance and Fracture Toughness of White Cast Iron Alloys, *Met. Mater. Int.*, 2016, **19**, p 473–481. https://doi.org/10.1007/s12540-013-3013-y

36. L.Y. Sheng, F. Yang, T.F. Xi, C. Lai, and H.Q. Ye, Influence of Heat Treatment on Interface of Cu/Al Bimetal Composite Fabricated by Cold Rolling, *Compos. Part B-Eng.*, 2011, **42**, p 1468–1473. https://doi.org/10.1016/j.compositesb.2011.04.045

37. H.R. Zareie Rajani, and S.A.A. Mousavi, The Effect of Explosive Welding Parameters on Metallurgical and Mechanical Interfacial

Features of Inconel 625/Plain Carbon Steel Bimetal Plate, *Mater. Sci. Eng. A*, 2012, **556**, p 454–464. https://doi.org/10.1016/j.msea.2012.07.012

38. H. Zhao, and L.Y. Sheng, Microstructure and Mechanical Properties of the Ag/316L Composite Plate Fabricated by Explosive Welding, *J. Manuf. Process.*, 2021, **64**, p 265–275. https://doi.org/10.1016/j.jmapro.2021.01.026

39. B.X. Liu, Q. An, F.X. Yin, S. Wang, and C.X. Chen, Interface Formation and Bonding Mechanisms of Hot-Rolled Tainless Steel Clad Plate, *J. Mater. Sci.*, 2019, **54**, p 11357–11377. https://doi.org/10.1007/s10853-019-03581-x

40. Y.C. Li, M.Y. Gong, K. Wang, P. Li, X. Yang, and W.P. Tong, Diffusion Behavior and Mechanical Properties of High Chromium Cast Iron/Low Carbon Steel Bimetal, *Mater. Sci. Eng. A*, 2018, **718**, p 260–266. https://doi.org/10.1016/j.msea.2018.01.111

41. Z.C. Luo, J.P. Ning, J. Wang, and K.H. Zheng, Microstructure and Wear Properties of TiC-Strengthened High-Manganese Steel Matrix Composites Fabricated by Hypereutectic Solidification, *Wear*, 2019 https://doi.org/10.1016/j.wear.2019.202970

42. T.X. Huang, Z. Li, Y.Q. Huang, Y. Li, and P. Xiao, Microstructure and Wear Properties of SiC Woodceramics Reinforced High-Chromium Cast Iron, *Ceram. Int.*, 2019, **46**, p 2592–2601. https://doi.org/10.1016/j.ceramint.2019.08.217